Seismically-induced unclogging in fluid-saturated faults

Nicolás D. Barbosa[1], Santiago G. Solazzi[2], Matteo Lupi[1].

[1]Department of Earth Sciences, University of Geneva, Geneva, Switzerland
[2]Institute of Earth Sciences, University of Lausanne, Lausanne, Switzerland
*

Key Points:

- We compute the magnitude of seismically-induced effective pore velocity to assess the unclogging potential in fluid-saturated fault zones
- Fluid pressure diffusion processes triggered by passing seismic waves are responsible of initiating unclogging in fault systems
- The unclogging mechanism operates at high frequencies and seismic strains but is controlled by the fault width and physical properties

Corresponding author: N. D. Barbosa, nicolas.barbosa@unige.ch
*Accepted for publication in JGR: Solid Earth.

Abstract

Evidence shows that flow-driven unclogging of pore spaces is correlated with permeability variations in fluid-saturated porous rocks. Due to the well-established ability of seismic waves to induce transient fluid flow in porous media, permeability changes due to seismically-induced unclogging have been proposed to explain hydrogeological phenomena commonly associated with distant earthquakes. In an effort to demonstrate the effects of seismically-induced unclogging, laboratory experiments of forced oscillatory flow in centimetre-scale samples have been performed. However, the corresponding extrapolation of the observations to the field scale has yet to be addressed. In this work, we model the coupling between the strains imposed by propagating seismic body waves and the development of transient flow in porous media following Biot's theory of poroelasticity. To assess the potential of seismically-induced unclogging, we use previously reported flow velocity thresholds for which measurable permeability variations were observed. We show that only diffusive waves can induce flow velocities in the order of those capable of initiating unclogging. In heterogeneous media, diffusive waves are created as energy conversion from passing seismic waves at the interfaces separating two porous phases of the medium. We investigate this mesoscale process for body waves propagating across a fault zone as a function of the energy density, frequency, and incidence angle of the waves. Seismically-induced unclogging potential in fault zones increases with frequency and imposed strain, although this relation is strongly affected by the incidence angle of the seismic wave, the fault thickness, and the stiffness contrast between the fault and the embedding background.

1 Introduction

Connected pores and fractures govern the flow of fluids in the subsurface. Fluid flow in porous media tends to carry colloids (e.g., fault gouge, precipitates, mineral grains, crushed proppants), which gradually clog flow paths, thus, decreasing the overall permeability of the rock formations (Wang et al., 2009; Manga et al., 2012). Correspondingly, the detachment from the surfaces of pores and mobilization of colloids (i.e., unclogging) associated with transient pore fluid pressure perturbations can enhance permeability as shown by field (Brodsky et al., 2003; Wang et al., 2009), laboratory (Bergendahl & Grasso, 2000; Li et al., 2005; Chen et al., 2018), and theoretical studies (Bai & Tien, 1997; Kutay & Aydilek, 2009; Bedrikovetsky et al., 2012). Seismic waves are capable of inducing strong pore pressure gradients in porous and fractured media due to the presence of regions with dissimilar stiffness such as, for example, a fault zone and the surrounding intact host rock (Müller et al., 2010; Pride et al., 2008; Barbosa, Hunziker, et al., 2019). Field observations suggest that permeability increases due to seismically induced unclogging can be of the order of 50% to 250% (Elkhoury et al., 2006; Xue et al., 2013). However, the conditions under which seismically-induced fluid flow is capable of initiating unclogging in the subsurface remain rather enigmatic.

As far as the authors know, mesoscale experiments investigating unclogging effects and carried out under well-controlled, reproducible, and comparable environmental conditions as those prevailing in field-scale reservoirs have not been performed. The only attempts to reproduce the unclogging effects of seismically-induced fluid flow have been performed at the lab scale, by imposing sinusoidal flow oscillations to fluid-saturated porous samples (Elkhoury et al., 2011; Candela et al., 2014). In both experimental studies, the flow was driven by oscillating the pore pressure on the top of a fluid-saturated Berea sandstone while holding the pore pressure constant at the bottom of the sample. The experiments showed that permeability of intact and fractured rocks can change as a result of transient changes in fluid flow. The permeability enhancement reported by Candela et al. (2014) ranged from 1 to 60% for measured strain amplitudes between 6×10^{-7} and 7×10^{-6}. The unclogging mechanism was proposed by Candela et al. (2014) to explain the permeability changes mainly based on the evidence of absence of permanent deformation of the sample after stimulation ceases (i.e., effects are not related to opening or closing of cracks), the direct observation of downstream mobilization of gouge particles along the fracture plane, and the recovery of the initial permeability after stimulation (i.e., reclogging of flow paths). Candela et al. (2015) pointed out that the permeability changes correlate with the volumetric averaged flow rate in the sample, regardless of whether flow rate variations are driven by varying pressure gradient amplitude or frequency of oscillation. Bedrikovetsky et al. (2012) showed that abrupt flow rate changes are particularly effective in mobilizing particles.

Previously reported experimental studies provide the basis for understanding the implications of seismically-induced permeability changes in the subsurface through unclogging. There is evidence to suggest that seismicity can be triggered by remarkably low dynamic stress levels associated with regional and distant earthquakes (well below 1 MPa), which, in turn, can be best explained by seismically-induced permeability enhancements (Brodsky et al., 2003; Brodsky & Prejean, 2005; Van Der Elst & Brodsky, 2010; Guglielmi et al., 2015; Lupi, Fuchs, & Saenger, 2017; Parsons et al., 2017). The unclogging mechanism has been proposed to be particularly relevant when gouge created during fracturing reduces the permeability and, thus, provokes an increase in pore pressure in a fault zone. In this scenario, seismic waves may break seals between compartments with different pressure, leading to a pressure re-equilibration and induced seismicity through effective stress changes (Xue et al., 2013; Parsons et al., 2017). Seismically-induced unclogging has also been evoked as a key mechanism for explaining other hydrogeological phenomena observed in the field after the passage of seismic waves from distant earthquakes. The most commonly reported example corresponds to co-seismic drops of the water level in wells (Brodsky et al., 2003; Elkhoury et al., 2006; Wang et al., 2009; Y. Shi et al., 2019).

The laboratory evidence also supports the stimulation of reservoirs with low-amplitude seismic stresses as a possible method for soft permeability enhancement, which could have a potential impact in areas such as, for example, geothermal and hydrocarbon resource exploitation, environmental remediation (Wang et al., 2009; Manga et al., 2012). Soft stimulation techniques aim at minimizing the level of induced seismicity while maximizing permeability enhancement and productivity. Examples of soft stimulation techniques include cyclic hydraulic fracturing, multi-stage hydraulic stimulation, chemical stimulation, and thermal stimulation (Huenges et al., 2018; Zang et al., 2019; Brehme et al., 2018). In view of this, and of the absence of relevant mesoscale experiments, a necessary first step towards understanding and predicting seismically-induced permeability changes due to unclogging either for naturally or artificially created seismic waves, is the extrapolation of small-scale laboratory experiments to the field scale (i.e., seismic wavelength scale). As mentioned before, faults are particularly interesting structures to study the potential of permeability enhancement through unclogging because pore pressure and effective stress changes, and, thus, fault stability, are highly affected by permeability variations.

In this work, we model the coupling between the shaking associated with the propagation of seismic waves and the development of transient pressure gradients in fluid-saturated fault zones. To do so, we follow Biot's theory of poroelasticity to model seismically-induced fluid flow in porous media and analyze the conditions under which seismic waves striking a fault can produce unclogging. We model both the fluid flow associated with the propagation of classical body waves (i.e., P- and S-waves) and diffusive slow P-waves. The latter are generally created by propagating seismic waves in the presence of heterogeneities such as, for example, faults or fractures, layering, patchy fluid saturation, as a result of the energy conversion prevailing at the interfaces between heterogeneities. To quantitatively assess the capability of the seismically-induced fluid flow to unclog pore spaces, we use theoretical and experimental results establishing threshold pore flow velocities for the occurence of unclogging. On this basis, we provide a comprehensive parametric analysis of the unclogging potential in a fault zone by varying petrophysical properties of the medium (e.g., fault stiffness contrast, porosity), seismic wave characteristics (e.g, wave mode, incidence angle, frequency, imposed strain), and fault thickness.

2 Methodology

In this section, we first present the dynamic equations of wave propagation in the context of poroelastic media. Then, we apply this theory to model seismically-induced fluid flow and to explain the experimental results in which permeability enhancement due to unclogging was observed (Candela et al., 2014).

2.1 Seismic wave propagation in the framework of Biot's theory of poroelasticity

Crustal rocks can be represented as porous media (Cheng, 2016), that is, a system composed of a skeletal material, herein referred to as the solid matrix, and a pore space, which is typically saturated with fluids. Biot's theory of poroelasticity (Biot, 1962) is the most widely adopted framework to investigate seismic wave propagation in fluid-saturated porous rocks. Assuming a porous medium characterized by an elastic and isotropic solid matrix, a single viscous fluid phase that is continuous throughout the pore-space, and small fluid and solid displacements, which is generally valid for seismic studies, the coupled equations describing seismic wave propagation in porous media in the space-frequency domain can be written as (Biot, 1962; Pride, 2005)

$$\boldsymbol{\tau}(\mathbf{u},\mathbf{w}) = 2\mu_m\boldsymbol{\varepsilon} + \mathbf{I}([K_u - \frac{2\mu_m}{3}]\nabla\cdot\mathbf{u} + \alpha M\nabla\cdot\mathbf{w}), \tag{1a}$$

$$p_f(\mathbf{u},\mathbf{w}) = -\alpha M\nabla\cdot\mathbf{u} - M\nabla\cdot\mathbf{w}, \tag{1b}$$

$$\nabla\cdot\boldsymbol{\tau} = -\omega^2\rho_b\mathbf{u} - \omega^2\rho_f\mathbf{w}, \tag{1c}$$

$$-\nabla p_f = -\omega^2\rho_f\mathbf{u} + i\omega\frac{\eta}{\kappa(\omega)}\mathbf{w}, \tag{1d}$$

where $\mathbf{I}$ is the identity matrix, i is the imaginary unit, and ω is the angular frequency. The poroelastic fields involved are the displacement of solid phase $\mathbf{u}$, the relative displacement of the fluid phase $\mathbf{w}$, the pore fluid pressure p_f, the total stress tensor $\boldsymbol{\tau}$, and the strain tensor $\boldsymbol{\varepsilon} = \frac{1}{2}(\nabla\mathbf{u}+(\nabla\mathbf{u})^T)$. Eqs. 1a and 1b correspond to the constitutive equations of the porous medium, Eq. 1c is the total balance of forces acting on the fluid-solid system, and Eq. 1d is the generalized Darcy's law of the relative fluid motion in the pores. The constitutive constants of an isotropic porous medium in Eqs. 1a and 1b are the shear modulus of the bulk material μ_m, the undrained bulk modulus K_u, the so-called Biot effective stress coefficient α, and the Biot fluid-storage modulus M, which can be obtained from the relations

$$\alpha = 1 - \frac{K_m}{K_s}, \tag{2a}$$

$$M = (\frac{\alpha-\phi}{K_s} + \frac{\phi}{K_f})^{-1}, \tag{2b}$$

where ϕ is the effective porosity of the matrix and K_s, $K_m = K_u - \alpha^2 M$, and K_f denote the bulk moduli of the solid grains, the dry matrix, and the pore fluid, respectively. The other properties characterising the fluid phase are the density ρ_f and shear viscosity η. The rest of the constants in the dynamic equations are the bulk density $\rho_b = (1-\phi)\rho_s+\phi\rho_f$, with ρ_s being the solid grains bulk modulus, and $\kappa(\omega)$ the dynamic permeability. The latter is a complex-valued frequency-dependent quantity describing the behavior of the relative fluid motion in the pores (Johnson et al., 1987). Its frequency dependence results from the fact that at relatively low and high frequencies, the drag that the solid matrix exerts on the fluid is dominated by viscous and inertial effects, respectively, and can be expressed as (Johnson et al., 1987; Pride, 2005)

$$\kappa_d(\omega) = \kappa\left(\sqrt{1+\frac{4i\omega}{n_j\omega_B}}+\frac{i\omega}{\omega_B}\right)^{-1}. \tag{3}$$

In Eq. 3, n_j is a parameter related to the permeability, the electrical formation factor, and the pore geometry of the rock. Johnson et al. (1987) also derived an expression for the characteristic frequency ω_B at which inertial forces dominate over viscous forces

$$\omega_B = \frac{\eta\phi}{\kappa_0 S\rho_f}, \tag{4}$$

where S is the tortuosity and κ_0 is the permeability typically employed to characterize fluid flow in porous media in the context of Darcy's law. We refer to ω_B as the Biot characteristic frequency, which in general is well above the seismic frequency band (Pride, 2005). Moreover, in this work, we assume (and verify using Eq. 4) that the frequencies at which unclogging takes place are in the frequency range where viscous forces dominate the flow in the pore space (i. e., $\omega \ll \omega_B$). As a result, the relative fluid motion is governed by Poiseuille flow and the dynamic permeability reduces to the real-valued hydraulic permeability κ_0.

A fundamental prediction of Biot's dynamic theory is that in addition to the classical body waves (S- and P-waves), a third wave mode commonly referred to as the slow P-wave propagates in porous media. The slow P-wave is a highly dispersive wave that, in the low-frequency regime, behaves as a diffusion process. In the presence of mesoscale heterogeneities, that is, heterogeneities whose characteristic size is much smaller than the seismic wavelength and much larger than the pore scale, the mechanical perturbation associated with the passing seismic wave-field induces fluid pressure gradients due to the stiffness contrast between the different porous phases of the medium. The fluid motion associated with the subsequent fluid pressure diffusion (FPD) process produces viscous friction at the pore scale, which, in turn, manifests itself in the form of attenuation and velocity dispersion in seismic records. This so-called mesoscopic wave-induced fluid flow phenomenon is a dominant attenuation mechanism in rocks of the shallower parts of the Earth's crust (Pride et al., 2004; Müller et al., 2010). The FPD process can be thought of as the body wave energy conversion at the interfaces of the heterogeneities to diffusive slow P-waves. Heterogeneous media can be described as a composition of piecewise homogeneous porous media (i.e, porous phases) for which Biot's equations are locally valid (White et al., 1975; Berryman & Wang, 2000; Pride & Berryman, 2003). In this kind of approach, Biot's equations are complemented by interface conditions relating the poroelastic fields on both sides of a surface separating two dissimilar phases (Deresiewicz & Skalak, 1963; Gurevich & Schoenberg, 1999).

2.2 The role of slow P-waves in permeability changes due to colloidal mobilization

Up to date, the only attempts to reproduce the effects of seismically-induced unclogging were performed in the laboratory and consisted of applying low-magnitude pore pressure changes on centimetre-scale rock samples (Roberts, 2005; Liu & Manga, 2009; Elkhoury et al., 2011; Kocharyan et al., 2011; Candela et al., 2014, 2015). In particular, Candela et al. (2014) computed permeability changes in intact and fractured water-saturated Berea sandstones while applying pore pressure oscillations at a frequency f=0.05 Hz. In the experiment, the authors first impose a driving-flow background pressure drop between the two ends of the probed sample, which is used to measure permeability. On top of the background pressure gradient, they apply pore pressure oscillations to study transient changes in the permeability of the sample. Red dots in Fig. 1a show the relation between the observed permeability changes and the ratio between the oscillatory pressure gradients and the background pressure gradient driving flow ("normalized pressure") for a water-saturated Berea sandstone.

Arguably the most important result of the work of Candela et al. (2014) is that the relative permeability enhancement is positively correlated with the normalized amplitude of pressure oscillations (Fig. 1). Although these results had been previously shown by Elkhoury et al. (2011) for fractured Berea sandstones, Candela et al. (2014) showed that this relation holds true for both intact and fractured rocks. In other words, colloidal mobilization driven by transient pressure changes can be an efficient method of permeability enhancement in porous media in general. The relation shown in Fig. 1 can be approximated by (Elkhoury et al., 2011)

$$\frac{\Delta\kappa}{\kappa_0} = a\left(\frac{\nabla p_f(\omega)}{\nabla p_f^0}\right)^b, \tag{5}$$

where $\Delta\kappa$ and κ_0 denote the absolute change in permeability and the initial permeability of the sample, respectively. $\nabla p_f(\omega)$ and ∇p_f^0, denote the oscillatory and background pressure gradients, respectively. The fitting parameters a and b in Elkhoury et al. (2011) were 0.7 and 1.7, respectively. We found that Eq. 5 also holds for the experiments of Candela et al. (2014) and estimated the fitting parameters to be $a = 0.42$ and $b = 1.96$.

In order to assess the ability of seismic waves to induce permeability changes such as those observed in Fig. 1, we compute the pressure gradients associated with slow P- and P-waves by solving Biot's equations in a homogeneous isotropic medium (see section 2.1). Most of the physical properties of the sample utilized by Candela et al. (2014) necessary for the poroelastic modelling are unknown. To estimate them, we use the reported permeability of the sample ($10^{-14.553}$ m^2) and assume a sample porosity in the order of 0.05 following relations reviewed by Bourbié et al. (1987) for clean sandstones. Note that if we follow the Kozeny-Carman relation ($\kappa = \beta d^2\phi^3/(1-\phi)^2$), the chosen permeability-porosity pair can be obtained by considering β=0.0009 (geometric factor) and a grain diameter d=150μm. We use the relations between porosity and matrix moduli proposed by Pride (2005), which are $K_m = K_s(1-\phi)/(1+c\phi)$ and $\mu_m = \mu_s(1-\phi)/(1+3c\phi/2)$, and we assume c=4 (consolidation parameter), K_s=37 GPa (grain bulk modulus), and μ_s=44 GPa (grain shear modulus). To quantify the tortuosity S in Eq. 4, we consider the relation $S = \phi^{1-m}$, with m being a cementation exponent equal to 1.5, which is typical of sandstones (Pride, 2005). For the parameter n_J in Eq. 3 we use a value of 8, which is also a common choice for sandstones (Pride, 2005). The full list of properties representative of a water-saturated Berea sandstone is given in Table 1. Regarding the characteristics of the waves, the pressure gradients were computed for strains of the same order of those measured by Candela et al. (2014), that is, between $\sim$5e-7 and $\sim$5e-6 and for a frequency of 0.05 Hz. Once the wave-induced pressure gradients are computed for slow P- and P-waves, we use Eq. 5 to model the associated permeability changes. In Eq. 5, we normalize the pressure gradients using ∇p_f^0= 4 MPa/m, which is representative of the experimental results of Candela et al. (2014) shown in Fig. 1. The very good agreement between the red dashed line and the dots in Fig. 1 implies that the effects observed by Candela et al. (2014) are mainly related to the action of diffusive slow P-waves. But more importantly, that the relative permeability changes associated with the classical P-waves are largely negligible compared with the effects associated with slow P-waves.

Gurevich et al. (1994) showed that, for frequencies below Biot's characteristic frequency (Eq. 4), which for the properties given in Table 1 is in the ultrasonic frequency range, the plane-wave solution of the set of Eqs. 1 can be approximated by the follow-

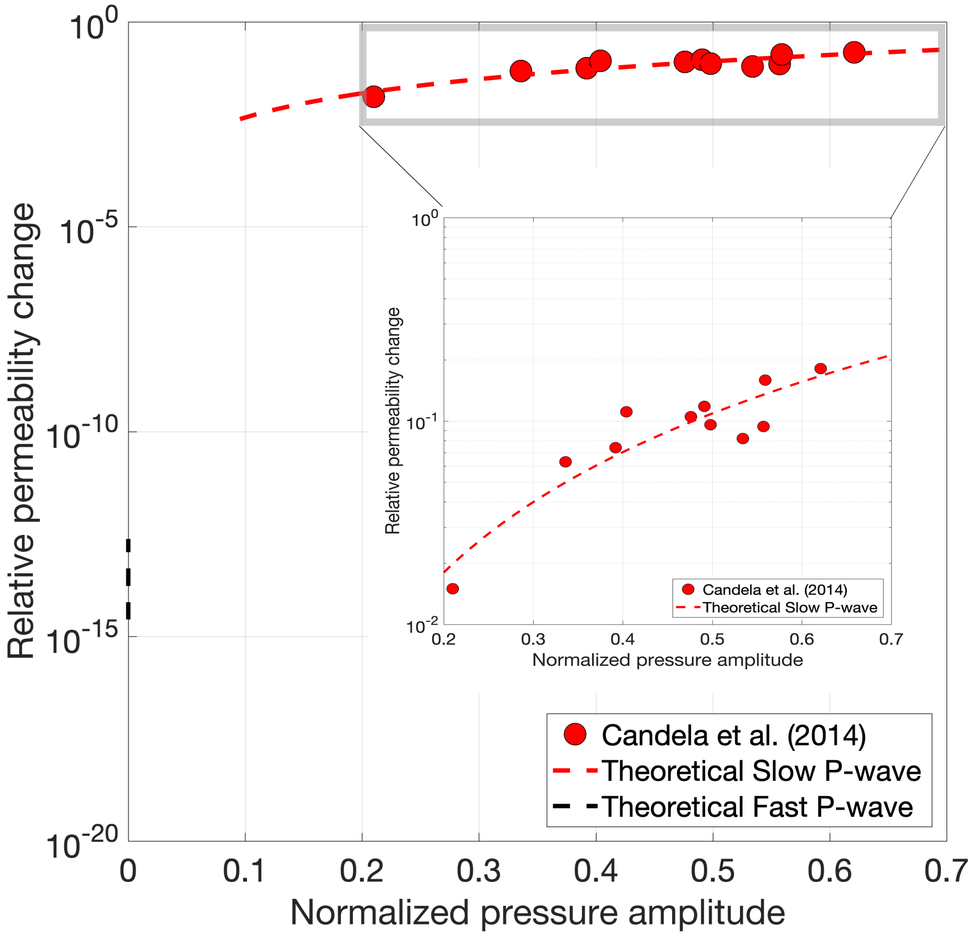

Figure 1. Theoretical predictions of the experiment of Candela et al. (2014) based on Biot's theory of poroelasticity. Red dots show the relation between imposed pressure oscillations normalized by the background pressure drop driving flow and the measured permeability changes in the sample from Candela et al. (2014). Red and black dashed lines denote permeability changes predicted for slow P- and P-waves (Eq. 5), respectively, as a function of the normalized pressure gradient created by each wave. The frequency of the waves is set to 0.05 Hz as in the experiment of Candela et al. (2014). The inset shows the prediction for the slow P-wave in more detail.

Table 1. Physical properties of a Berea sandstone utilized for the analysis of normalized pore pressure changes as function of seismic strains of slow P- and P-waves.

	Berea sandstone
Grain bulk modulus (K_s)	37 [GPa]
Grain shear modulus (μ_s)	44 [GPa]
Grain density (ρ_s)	2650 [kg/m^3]
Matrix bulk modulus (K_m)	29.3 [GPa]
Matrix shear modulus (μ_m)	32.15 [GPa]
Porosity (ϕ)	0.05 [-]
Permeability (κ)	0.0028 [D]
Fluid Viscosity (η)	0.0016 [Pa·s]
Fluid bulk modulus (K_f)	2.25 [GPa]
Fluid density (ρ_f)	1090 [kg/m^3]
Tortuosity (S)	$\phi^{0.5}$
n_J	8

ing wave-numbers (k)

$$k_P \simeq \frac{\omega}{V_P}, \tag{6}$$

$$k_S \simeq \frac{\omega}{V_S}, \tag{7}$$

$$k_{P_{slow}} \simeq \frac{\sqrt{-i}}{L_D}, \tag{8}$$

where $V_S = \sqrt{\frac{\mu_m}{\rho_b}}$ and $V_P = \sqrt{\frac{H_u}{\rho_b}}$ correspond to the S- and P-wave velocities in the low-frequency regime, respectively, with $H_u = K_u + 4/3\mu_m$. The diffusion length in the equation of the slow P-wavenumber (denoted by P_{slow} in Eq. 8) is

$$L_D = \sqrt{\frac{D}{\omega}}, \tag{9}$$

with $D = \frac{\kappa}{\eta}\left(M - \frac{\alpha^2 M^2}{H_u}\right)$ denoting the diffusivity of the medium. L_D is the distance at which the amplitude of the pore pressure induced by the slow P-wave decays approximately by half. It is well known that, for frequencies in the seismic range, slow P-wave effects are negligible a few meters away from their source (Pride et al., 2008). This condition implies that even if it were possible to create slow P-waves with relatively high seismic strains (e.g., in a stimulation well), the energy of these waves would decay and become negligible rapidly (i.e., L_D can be of the order of a few meters at most). Correspondingly, permeability changes due to seismically-induced colloidal mobilization are limited to the vicinity of the source of the diffusive waves. Far from the seismic source ($r \gg 1$ m), the seismic energy can only be carried by P- and S-waves, which, in turn, produce negligible effects on colloidal mobilization (Fig. 1). However, as mentioned in Section 2.1, when P- and S-waves propagate through a medium exhibiting stiffness contrasts (e.g., due to layering, fracturing, patchy distribution of fluids, etc), additional pressure gradients, which equilibrate through FPD, are created by the passing waves. In other words, slow P-waves are created at the interface between two dissimilar porous phases of the medium. In such scenario, provided the seismic energy of the incident wave is high enough, the effects of the triggered diffusive waves may be sufficiently large to unclog regions of the pore space and change permeability. In this work, we address this question in the particular case of P- and S-waves striking a fault zone.

Table 2. Minimum effective pore fluid velocity correlated with observable effects of unclogging in porous media.

Authors	v_{eff} **[mm/s]**	**Origin**
Bergendahl and Grasso (2000)	1.82	Flow through porous medium
Brodsky et al. (2003)	1	Rayleigh waves
Wang et al. (2009)	0.2-0.9	S and Love waves dynamic strains
Kocharyan et al. (2011)	0.5-1	Surface waves
Candela et al. (2014), Candela et al. (2015)	0.1-1	Controlled pressure oscillations

2.3 Criterion for initiation of unclogging

In this section, we define a criterion for which unclogging is expected to take place and produce observable effects on permeability. Assuming that unclogging initiates by rolling of colloids, it is expected to occur when the resistance to rolling is overcome by the applied moment from hydrodynamic forces (Bergendahl & Grasso, 2000). For a Poiseuille-type fluid flow in the pores (i.e., frequencies in the seismic range and below), the hydrodynamic shear experienced by a colloid attached to a pore wall is proportional to the effective pore velocity v_{eff} defined as (Bergendahl & Grasso, 2000; Brodsky et al., 2003)

$$v_{eff} = \frac{Q}{\phi A_{cross}} = \frac{\dot{w}}{\phi}, \tag{10}$$

where Q is the flow rate across an area A_{cross} of the porous medium and $\dot{w}$ is the magnitude of the fluid velocity relative to the solid matrix in a unit volume of porous medium. High pore velocities generated due to the presence of large local pressure gradients, producing large Q values, directly affect the magnitude of the hydrodynamic shear acting on the colloids. It is important to mention that the latter is also a function of the effective pore diameter and the colloidal radius (Bergendahl & Grasso, 2000). Eq. 10 is particularly useful because it links the fluid motion at the pore scale (v_{eff}) with macroscopic quantities such as Q and $\dot{w}$. In particular, the fluid relative velocity $\dot{w}$ is a poroelastic variable that can be computed from the pressure gradients imposed by propagating seismic waves (magnitude of the time derivative of $\mathbf{w}$ in the set of Eqs. 1).

In Table 2, we provide a list of experimental studies in which unclogging in porous media has been observed or inferred and the corresponding estimated pore fluid velocity. Bergendahl and Grasso (2000) presented a mathematical model to predict hydrodynamic conditions leading to initiation of colloidal detachment in a porous medium using a constricted tube model. In addition, the authors performed a fluid flow experiment across a column of porous medium while increasing the flow rate sequentially from 5 to

100 ml min^{-1}. A spectrophotometer provided continuous optical density readings, which were converted to concentration of colloids. The authors quantified the hydrodynamic forces in the fluid that explained the observed colloidal removal-flow rate relation. Bergendahl and Grasso (2000) observed colloidal mobilization at flow rates above 30 ml/s, corresponding to v_{eff}=1.82 mm/s. In the case of transient fluid motion, Wang et al. (2009) estimated that v_{eff} must be greater or equal than 0.03 mm/s in order to create sufficient hydrodynamic shearing to initiate unclogging. They found that at an epicentral distance of ∼2000 km of a magnitude 7.9 earthquake, oscillatory groundwater flow associated with passing Rayleigh, Love, and S-waves was strong enough (0.2 to 0.9 mm/s) to unclog pores and increase aquifer permeability. Brodsky et al. (2003) and Kocharyan et al. (2011) estimated that pore fluid velocities of the order of 1 mm/s were sufficient to unclog large fractures based on water level changes in wells in response to the passage of surface waves. Using Eq. 10, we have estimated the effective pore fluid velocity for the oscillatory pressure experiments of Candela et al. (2014) to be in the range 0.1-1 mm/s by taking representative values of Q of their experiment between $10^{-7.5}$ and 10^{-8}m^3/s for $A_{cross} =$ 45×29 mm^2. Based on the above-mentioned evidence, in this work we assume a threshold value for v_{eff} of 0.1 mm/s in order to quantitatively assess the feasibility of seismically-induced unclogging in fluid-saturated porous media.

We note here that seismically-induced changes in physical properties of the medium are not quantified or accounted for in this work. In particular, permeability changes are not modeled for various reasons. First, as far as the authors know, there are no analytical or empirical models relating permeability changes through unclogging with seismically-induced fluid flow. The empirical laws given by Elkhoury et al. (2011) and Candela et al. (2015) for Berea sandstones are not universal but are meant to explain the results of pressure oscillation experiments on small scale samples in which a background flow is perturbed by harmonically oscillating the pore pressure. Moreover, empirical laws such as the one given in Eq. 5 require knowledge of (and are scaled by) the static background pressure gradient. Second, according to Roberts and Abdel-Fattah (2009), different types of colloidal mobilization can follow an abrupt change in fluid flow, including detachment from pore walls, expulsion from dead-end pores, and pore throat fouling breakup. The latter case is expected to induce the largest permeability variations but, a priori, it is not possible to quantify and differentiate the corresponding effects. Third, unclogging effects on permeability sometimes operate with other mechanisms affecting permeability. In fractured rocks, a prominent example is when the seismic stressing produces permanent deformation associated with a change in fracture aperture (Liu & Manga, 2009; Shokouhi et al., 2019). The interrelation between different mechanisms can cause permeability to either increase or decrease (Z. Shi et al., 2018; Y. Shi et al., 2019). For these reasons, in this work, we focus on analyzing the ability of seismic waves to initiate unclogging.

3 Seismically-induced unclogging in faults

3.1 Single-layer scattering problem

In this section, we study how energy is converted from P- and S-waves into slow P-waves when the former propagate across a fluid-saturated fault zone. By conceptualizing the fault zone as an isotropic, compliant layer embedded in a stiffer background medium (i.e., the host rock), the problem reduces to modelling the scattering of seismic waves at a single layer. Fig. 2 illustrates the reflected and transmitted wave-fields at a single layer for the case of P-wave normal incidence. We consider the Cartesian coordinate system shown in Fig. 2, which allows us to study the wave propagation in the x-y plane while wave propagation in the z-direction is not considered. We use the methodology described in Barbosa et al. (2016) to compute the amplitudes of the scattered wave fields for P- and S-wave incidence at arbitrary incidence angles. We acknowledge that, in general, faults have complex architectures involving damage zones surrounding a fault

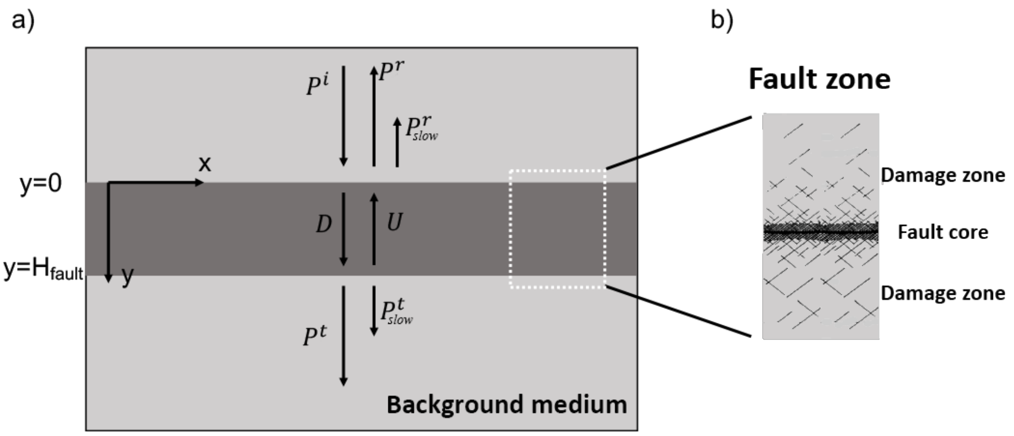

Figure 2. Schematic illustration of the fault reflectivity problem for normal P-wave incidence. a) The arrows indicate the positive directions of wave propagation. P and P_{slow} refer to the P- and slow P-waves, respectively. The superscripts r and t denote reflected and transmitted waves in the background medium, respectively. Letters D and U denote down-going and up-going wave fields inside the fault, respectively. We consider an isotropic, compliant, poroelastic layer representing a fault, which is a simplification of a fault zone composed by a fault core surrounded by a damage zone (b). Fault structure adapted from Chester et al. (1993). The fault is embedded in a background medium having similar properties to those of the Berea sandstone utilized by Candela et al. (2014).

core (Fig. 2b). This implies that pressure gradients can be created not only at the interface between the fault as a whole but also within mesoscale heterogeneities inside the fault zone that are larger than the pore size but smaller than the size of the fault (e.g., interconnected fractures as shown in Barbosa, Hunziker, et al. (2019)). Under the assumption that frequencies are low enough so that fluid pressure has enough time to equilibrate between heterogeneities within the fault zone during the passage of the seismic wave (“relaxed state”), we can approximate the response of the fault zone with the one of an effective poroelastic layer as in Fig. 2a. Given that the interior of the fault is composed of fractures and background medium, the assumption above is valid as long as the diffusion length of the slow P-waves inside the fault zone is much larger than the characteristic size of the fractures. Within the validity of this model, we can assess the magnitude of the seismically-induced fluid flow, and the corresponding unclogging potential, associated with the slow P-waves created when seismic waves propagate through the fault zone.

3.1.1 Fault properties

At given seismic wave frequency and strain, the amplitude of the slow P-waves created at the interfaces of the fault (Fig. 2a) is controlled by the mechanical and hydraulic contrast between the fault and the embedding medium, and by the thickness of the fault zone. In order to parameterize the stiffness contrast between the fault and the embedding background medium we use the following relations

$$K_m^{fault} = K_m^b/\alpha, \tag{11}$$

$$\mu_m^{fault} = \mu_m^b/\beta, \tag{12}$$

Table 3. Physical properties of the fault, which are related to the properties of the background. Given that both fault and background properties are characterized as a function of background porosity, we show the velocity associated with each porosity value used in the study.

	Stiff fault	**Soft fault**
P-wave velocity (V_p)	4670 [m/s]	2610 [m/s] ($\phi^b = 0.05$)
	4205 [m/s]	2460 [m/s] ($\phi^b = 0.1$)
	3850 [m/s]	2350 [m/s] ($\phi^b = 0.15$)
S-wave velocity (V_s)	3050 [m/s]	1450 [m/s] ($\phi^b = 0.05$)
	2680 [m/s]	1275 [m/s] ($\phi^b = 0.1$)
	2390 [m/s]	1140 [m/s] ($\phi^b = 0.15$)
Bulk density (ρ_b)	2275 [kg/m^3]	2275 [kg/m^3]
E^b/E^{fault}	1.5	$\sim$8

with α and β dimensionless parameters larger than 1. For our analysis, we assume two possible relations to define the elastic properties of the fault layer: (a) α=12.5, β=6.6, which in the following is referred to as the "soft fault"; and (b) a "stiff fault" case with α=β=1.5. It is important to note that the properties of the fault depend on the properties of the background medium. In the following, in those cases where the background properties are changed, the fault elastic moduli are changed according to Eqs. 11 and 12. Table 3 summarizes the range of variation of the properties of the soft and stiff faults considered in this work. Jeanne et al. (2017) provide measurements as well as a compilation of literature values of Young modulus (E) variations along faults from the background medium to the fault core. Jeanne et al. (2017) showed that the factor decay of the Young modulus (E^b/E^{fc}) from the host rock (superscript b) to the fault core (superscript fc) can vary between 1.5 and 12.5. Table 3 shows that both for the soft and stiff faults, this ratio is in the range of the observations of Jeanne et al. (2017). Further, the properties chosen for the soft fault case, representing the largest compressibility contrast, are in the range of those used by Lupi et al. (2013) to model faults in the Lusi mud eruption and its hydrothermal system (V_p=2325 m/s, V_s=1531 m/s, and ρ_b=2000 kg/m^3). Note that the above-mentioned works, and thus the fault properties given in Table 3, provide values representative of upper-crust structures (i.e, up to few kilometers depth). Regarding the hydraulic contrast between the fault and the background, we have fixed the porosity and permeability of the fault to 0.25 and 0.5e-12 m^2 ($\sim$ 0.5 D), respectively. For all cases, the fault is more permeable and with higher diffusivity than the embedding background medium. As a reference scenario, the background medium has the properties of the Berea sandstone listed in Table 1, but we also consider other two cases in which the background porosity is increased to 0.1 and 0.15. For these additional cases, the permeability and elastic moduli of the background are defined from the background porosity values following the same relations described in Section 2.2. Finally, the grain and fluid properties in the fault are assumed to be the same as in the background medium (Table 1). It is important to remark that for the background and fault properties described above, ω_B (Eq. 4) is always in the sonic to ultrasonic frequency range.

We assume reference scenarios for the fault zone thickness between 0.1 m and 1 m. For the soft fault properties given in Table 3 and a fault thickness of 0.1 m, the dry normal (η_N=$H_{fault}/(K_m$+$4/3\mu_m)$) and tangential compliances (η_T=H_{fault}/μ_m) characterizing the mechanical response of the faults are in the range [1.1-1.8]$\times10^{-11}$m/Pa and [2-3.3]$\times10^{-11}$m/Pa, respectively. These compliance values are in the order of those expected for faults of tens of meters lengths according to the corresponding relation shown in previous works (Hobday & Worthington, 2012; Barbosa, Caspari, et al., 2019). From a structural point of view, a fault zone thickness of 0.1 m corresponds to a fault displacement of the same order (Faulkner et al., 2011; Savage & Brodsky, 2011). Using the empirical relation between fault displacement and fault length reviewed by Kim and Sanderson (2005), fault lengths are expected to be in the order of tens of meters, which is consistent with the fault mechanical properties considered.

3.1.2 Seismic wave properties

The fluid flow associated with slow P-waves is also a function of the strain and frequency of the incident P- or S-wave. To define an upper bound for the seismic strain, we follow the results of Lupi et al. (2013) and Lupi, Frehner, et al. (2017) on dynamic processes associated with the passage of body waves released from regional earthquakes. In these studies, seismic strains of up to 2e-5 for frequencies around 1 Hz were inferred from dynamic displacements recorded at the surface. For our study, we consider seismic strains (ε) in the range of 1e-6 to 1e-5. We consider frequencies between 0.1 and 20 Hz, which, together with the chosen strain values, cover the typical ranges used in laboratory experiments investigating unclogging as well as those observed for seismic waves associated with regional events. Using that $\varepsilon = iuk$, where u is the seismically-induced solid displacement, the maximum seismic wave energy density e can be computed as $\rho_b(\varepsilon\omega/2k)^2$ (Lay & Wallace, 1995). Considering Eqs. 6 and 7, it follows that $e_P = \rho_b(\varepsilon V_P/2)^2$ and $e_S = \rho_b(\varepsilon V_S/2)^2$, which are independent of the frequency. For the strains considered above, e_P and e_S range from 0.01 J/m^3 to 1 J/m^3. These values are within the typical range at which regional earthquakes can induce water level in wells and spring temperature changes (Wang & Manga, 2010). In the following, we analyze first the case of normal P-wave incidence and then generalize the analysis to P- and S-wave oblique incidence.

3.2 Normal P-wave incidence

The fault seismic reflectivity problem illustrated in Fig. 2 represents an upscaled field analogue to the laboratory experiment of Candela et al. (2014) in which slow P-waves are created as a result of scattering of the seismic wave energy of an incident body wave. Fig. 3 shows the frequency dependence of the effective pore velocity (Eq. 10) associated with the scattered slow P-waves at the fault interface y=0 m (Fig. 2) and propagating into the host medium (P^r_{slow} in Fig. 2) and into the fault (associated with both downgoing D and up-going U fields in Fig. 2). As a reference, we plot the threshold effective pore velocity v^0_{eff} (red dashed line) adopted for this work. We consider three sets of properties for the background medium, which are parameterized as functions of the porosity. For this, we consider ϕ_1=0.05, ϕ_2=0.1, and ϕ_3=0.15 (ϕ=0.05 corresponds to the properties given in Table 1). The fault properties are those corresponding to the soft fault in Table 3 and the thickness H_{fault} is set to 0.1 m.

Let us first analyze the sensitivity of v_{eff} associated with the slow P-waves to the strain of the incident P-wave. We consider incident P-wave strains equal to 1e-6 (Fig. 3a) and 1e-5 (Fig. 3b). Fig. 3 shows that v_{eff} inside the fault increases with the background porosity. Given that faults are parameterized in a way such that only their elastic properties are allowed to change, the dependence of v_{eff} with background porosity inside the fault implies that the compressibility contrast between the fault and embedding background is effectively maximal for the case of 0.15 porosity. Furthermore, the sensitivity of v_{eff} to the changes in properties is more important in the fault than in the background medium (compare dashed and solid lines in Fig. 3). In general, slow P-waves induce higher v_{eff} towards the background medium than inside the fault. This suggests that unclogging is more likely to be more efficient from the background to the fault than inside the fault. At a given strain magnitude, v_{eff} increases with the frequency and its frequency dependence in the fault and in the background medium is similar. Regarding

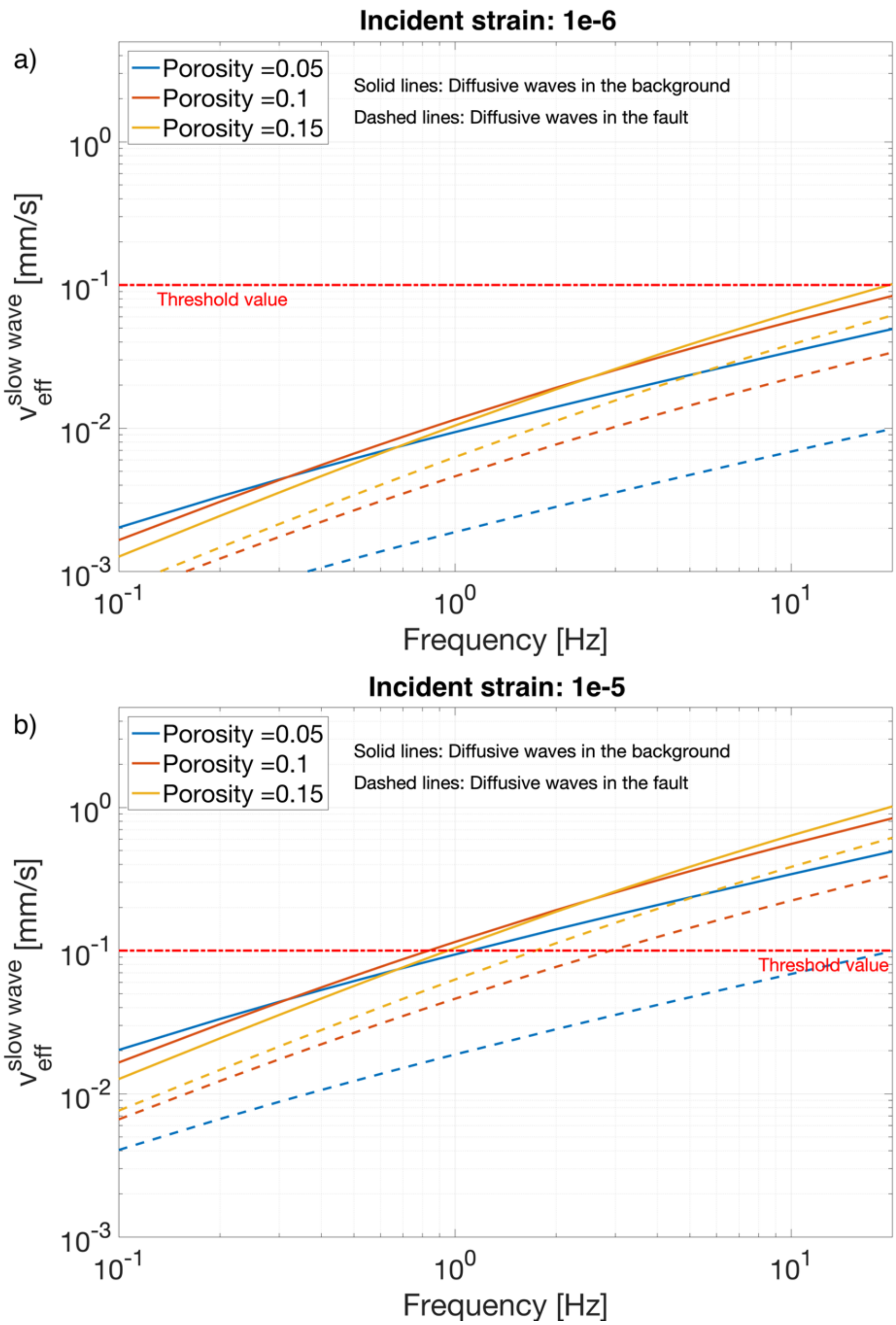

Figure 3. Effective pore velocity in the fault (dashed lines) and in the background medium (solid lines) as a function of frequency for normal P-wave incidence. The red dashed line denotes the threshold value v_{eff}^0 above which unclogging has been observed in other studies. Incident strain is equal to a) 1e-6 and b) 1e-5. Fault thickness is 0.1 m. v_{eff} tends to be smaller in fault that in the background due to the larger fault diffusivity.

the effect of the incident strain, an order of magnitude increase in seismic strain results in an order of magnitude increase in v_{eff}. For 1e-6 incident strain, the threshold value

(v_{eff}=0.1 mm/s) is reached neither in the background nor the fault. For 1e-5 incident strain, v_{eff} is above the threshold for frequencies above 1 Hz and all cases considered both inside the fault and in the background medium, except for the case of porosity equal to 0.05 (Fig. 3b). Note that the curves in Fig. 3a and Fig. 3b represent the response for incident seismic energy densities close to 0.01 J/m^3 and 1 J/m^3, respectively, regardless of the frequency considered. These results show that the strain of the incident wave is a key parameter controlling the seismically-induced unclogging potential in fault zones.

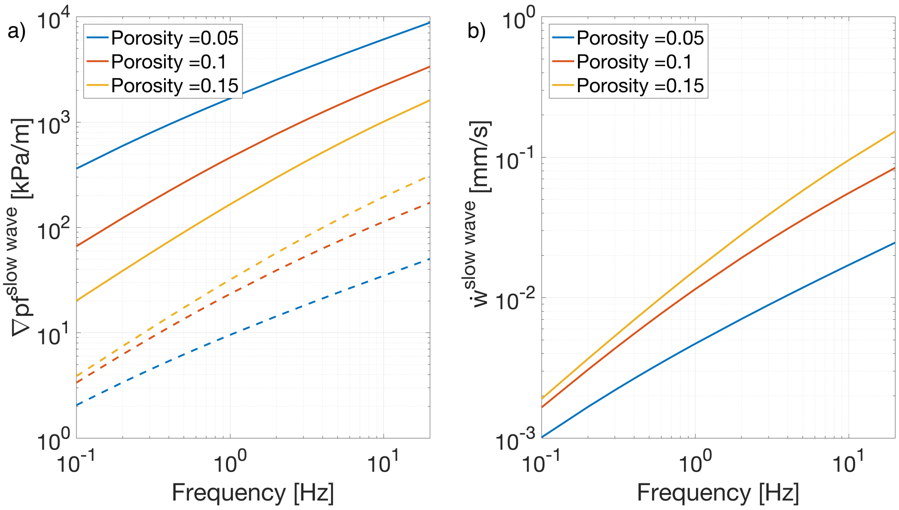

Figure 4. (a) Pressure gradient and (b) Darcy velocity associated with the slow P-wave as functions of frequency. The pressure gradient is computed at the interface between the background (solid lines) and the fault (dashed lines). The strain of the incident P-wave and the petrophysical properties are those used in Fig. 3b.

To better understand the seismically-induced v_{eff}, Fig. 4 shows the frequency dependence of the fluid pressure gradient and Darcy velocity at the interface between the background medium and the fault. The properties of the incident wave, as well as those of the medium, are the same as in Fig. 3b. In the background medium, the incidence of P-waves at the fault is able to induce particularly strong pressure gradients. As a consequence, transient pressure gradients associated with the FPD (e.g., blue curve in Fig. 4a) can be several orders of magnitude higher than natural pressure gradients producing an effective velocity of ∼5 m/day in conductive fractures (Brodsky et al., 2003; Kocharyan et al., 2011), which are in the order of several kPa/m. In the background medium, the highest pressure gradients occur for the model with 0.05 porosity but this model produces the lowest Darcy velocity (Fig. 4b). This is due to the fact that the Darcy velocity is not only proportional to the pressure gradient but also to the permeability of the medium, which is smaller for the case of 0.05 porosity. In the fault, the pressure gradients associated with the FPD process are smaller due to its higher diffusivity. Unlike in the background, the pressure gradients increase with the porosity of the host rock. As mentioned before, given that the fault hydraulic properties are the same in the three cases, this observation implies that the compressibility contrast between the fault and the embedding background effectively increases with the background porosity. Based on the comparison between Fig. 3b and Fig. 4a, pressure gradients of the order of hundreds of kPa/m are necessary to reach v^0_{eff} in the background and in the fault. Note that the pressure gradients imposed in laboratory experiments are in this range (Elkhoury et al., 2011; Candela et al., 2014, 2015).

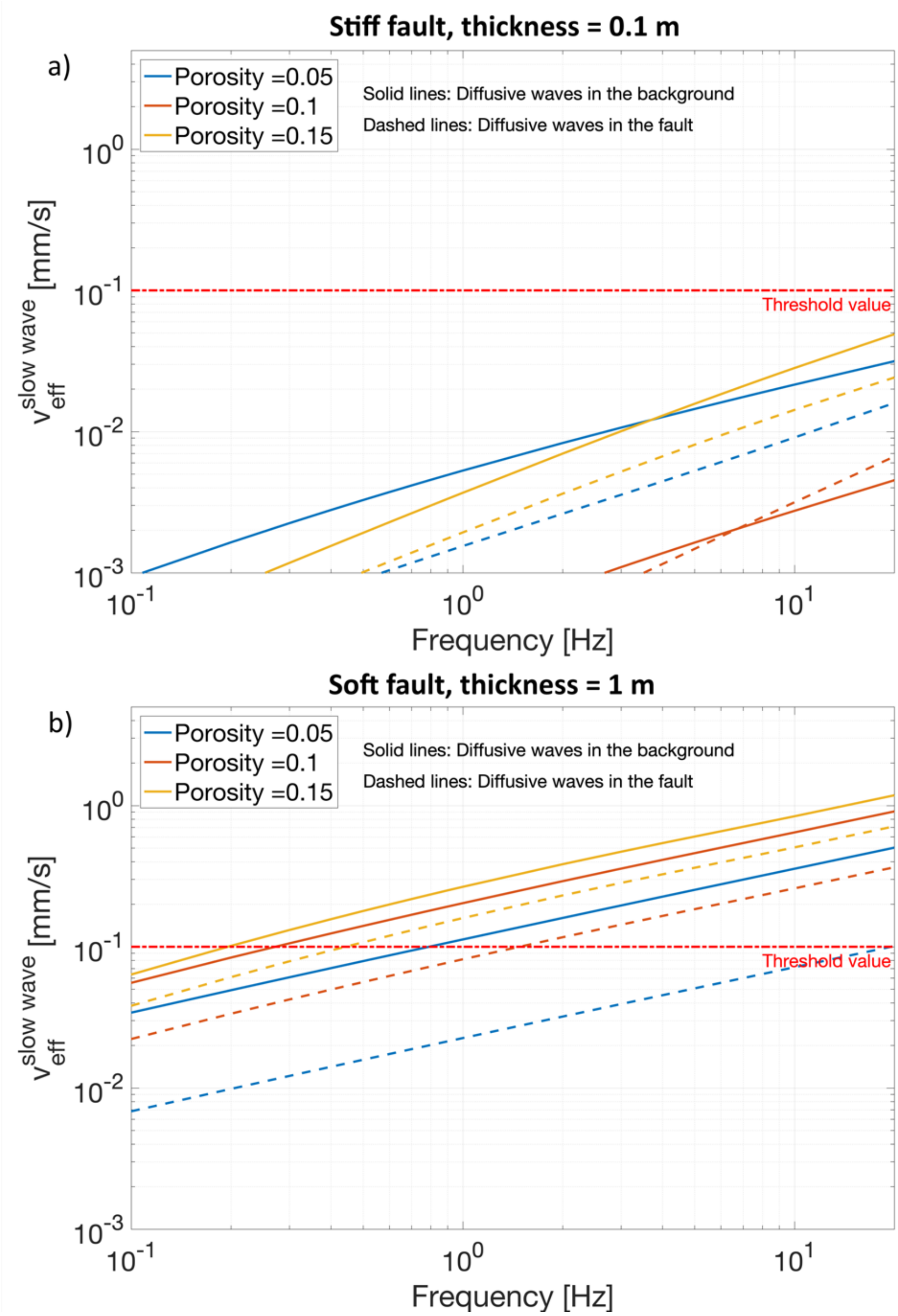

Figure 5. Effective pore velocity in the fault and in the background medium as a function of frequency for normal P-wave incidence. The red dashed line denotes the threshold value of v^0_{eff}=0.1 mm/s. Panels a) and b) correspond to a 0.1 m thick stiff fault and a 1 m thick soft fault, respectively.

As previously noted, another critical parameter for the magnitude of the seismically-induced pressure gradients is the fault compliance, which relates to its elastic moduli and thickness. In order to illustrate the effect of fault compliance on v_{eff}, in Fig. 5a, we consider a fault with the stiff properties given in Table 3. For a 0.1 m thick fault, the compliances η_N and η_T are in the range [0.21-0.33]$\times 10^{-11}$m/Pa and [0.47-0.76]$\times 10^{-11}$m/Pa, respectively. That is, the compliance of the stiff fault is approximately one order of magnitude lower than the soft fault that was analyzed up until now. In Fig. 5a we consider an incident strain of 1e-5 ($e_P \sim 1$ J/m^3), which was the most favorable case in Fig. 3. As expected, the compressibility contrast between the fault and the embedding medium plays a major role in the magnitude of v_{eff} associated with the scattered slow P-waves. A stiff fault is associated with v_{eff} values below v^0_{eff} regardless of the frequency of the wave, which implies that its unclogging potential is much lower than for the considered soft faults. Note also that the behavior of v_{eff} with changing porosity is not as direct as for the soft fault (Fig. 3b).

Fig. 5b shows the case of a 1 m thick fault with the soft properties given in Table 3. Due to the increase in H_{fault}, the fault in Fig. 5b represents an order of magnitude increase in effective compliance with respect to the one in Fig. 3b and, in turn, is representative of tens to hundreds of meters length faults (Kim & Sanderson, 2005; Faulkner et al., 2011; Savage & Brodsky, 2011). Although background properties in Figs. 3b and 5b are the same, the larger thickness and compliance of the fault considered in Fig. 5b with respect to those considered in Fig. 3b result in significantly higher v_{eff} both in the interior of the fault and in the background medium. As a result, for example, in Fig. 5b values of v_{eff} above 0.1 mm/s are reached below 1 Hz. The reason for this increase is that the energy conversion from the incident P-wave to slow P-waves at the edge of the fault depends on the ratio between the incident wavelength and the thickness of the fault. As the ratio increases, the reflectivity of the fault decreases. For a fault thickness of 1 m, the amplitude of the converted slow P-waves and, consequently, the induced v_{eff} is larger than the values obtained for 0.1 m. This implies that if the thickness of the fault changes along its plane, unclogging effects are expected to occur in the thickest sections. However, in a poroelastic approach, the reflectivity of a layer depends not only on the ratio between the wavelength and the thickness but, also, on the relation between the wave frequency and the characteristic frequency of the mesoscopic FPD process occurring between the fault and the background medium (f_c). An example of these competing effects can be observed by comparing the responses for the 0.1 m soft fault (Fig. 3b) and the 1 m stiff fault (Fig. 5b) when the background porosity is 0.05. We observe that they are practically identical. This similarity implies that the magnitude of v_{eff} depends both on H_{fault} and f_c.

Fig. 6 provides further details on the relation between v_{eff} and the thickness of the fault. Top and bottom panels of Fig. 6 correspond to fixed frequencies of 0.1 Hz and 1 Hz, respectively. The fault properties are equal to the soft fault properties given in Table 3 regardless of the thickness of the fault. We observe that as H_{fault} increases, v_{eff} at the interface between the fault and the background increases. However, at some point the value of v_{eff} stabilizes. The thickness at which the curves change their slope can be estimated from f_c, which is given by (Müller & Rothert, 2006)

$$\omega_c = 2\pi f_c = \left(\frac{2}{H_{fault}}\right)^2 D^{fault}_{eff}, \tag{13}$$

where the effective fault diffusivity D^{fault}_{eff} is defined as

$$D^{fault}_{eff} = \left(\frac{e_b^2}{e_f^2 + e_f e_b}\right) D^f, \tag{14}$$

with the effusivity

$$e = \frac{\kappa}{\eta\sqrt{D}}. \tag{15}$$

In Eqs. 14 and 15, the subscripts b and f refer to background and fault properties, respectively. From Eqs. 9 and 13, it is clear that ω_c is related to an effective diffusion length

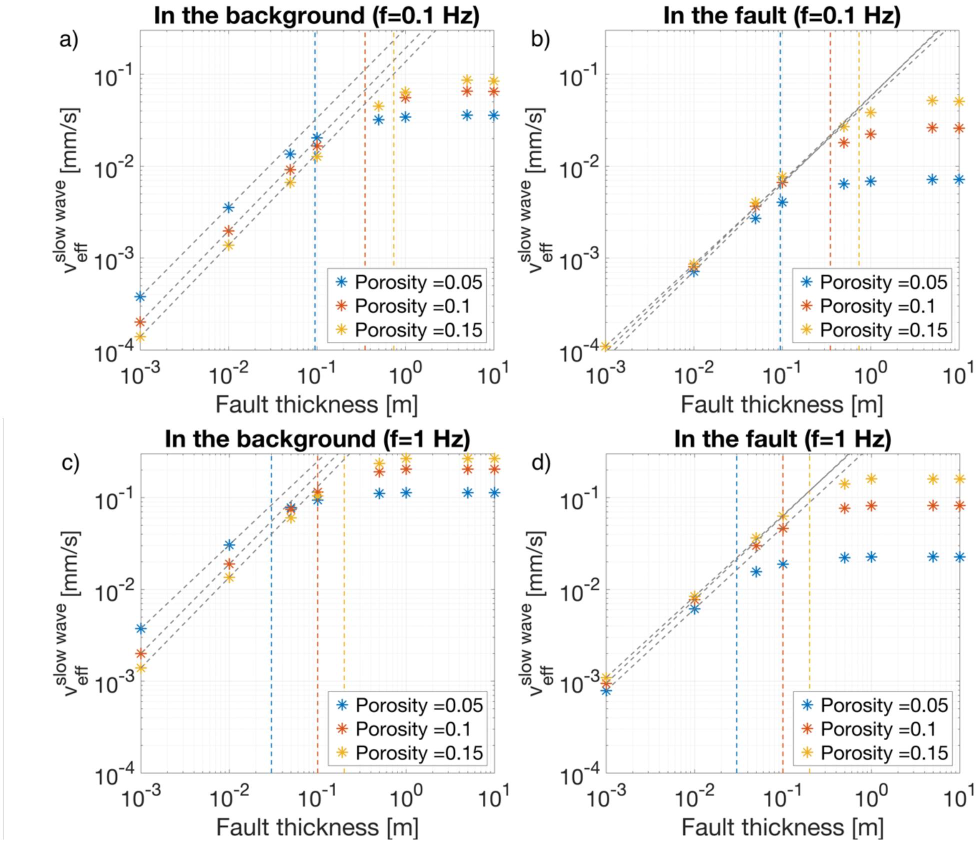

Figure 6. Effective pore velocity in the fault and in the background medium as a function of fault thickness for normal P-wave incidence. Top and bottom panels correspond to seismic wave frequencies of 0.1 Hz and 1 Hz, respectively.

L_{eff} equal to half the fault thickness. In Fig. 6, we have computed the fault thickness at which f_c is equal to 0.1 Hz and 1 Hz for the different scenarios defined by the background porosity values. In other words, we have computed the minimum fault thickness for which the diffusion process inside the fault can fully develop for the considered frequency. The corresponding thickness values are plotted in Fig. 6 with vertical dashed lines and colors denoting the different porosity cases. We observe that for 0.1 Hz, the thickness at which the slope of the curves decreases is between 0.1 m and 1 m. For 1 Hz, the curves approach the flat regime at smaller thicknesses. There is good agreement between the thickness values computed using Eq. 13 for the different frequencies considered and the inflection points of the curves. This means that we can interpret the lack of sensitivity of v_{eff} to the fault thickness as the latter becoming larger than two diffusion lengths inside the fault.

Recall that the values shown in Figs. 3 to 6 correspond to those induced at one of the fault's edges (y=0 m in Fig. 2). As the slow P-wave travels into the background medium or the fault zone, its amplitude and the corresponding unclogging potential decay. The associated effects for a 0.1 m and 1 m thick fault for three frequencies are shown in Fig. 7. The seismic strain is fixed to 1e-5 regardless of the frequency considered. For illustration purposes, we only consider one of the scenarios shown in Figs. 3 to 5, which corresponds to a soft fault embedded in a background with a porosity of 0.15 (the most favorable case for unclogging). Eq. 9 shows that as the frequency of the incident wave increases, the diffusion length decreases, which is translated in Fig. 7 to a sharper decrease

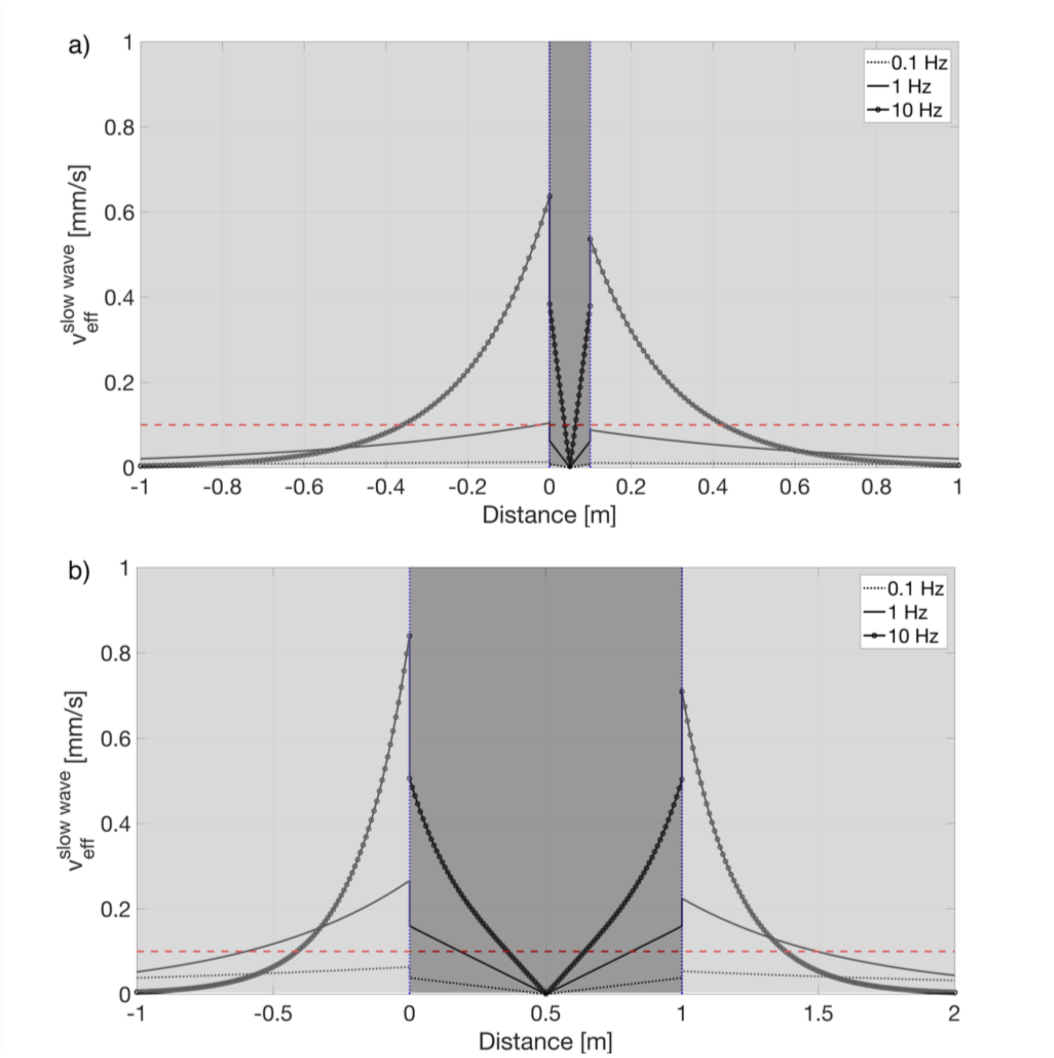

Figure 7. Effective pore velocity profile across the fault for normal P-wave incidence. The red dashed line denotes the threshold value of v^0_{eff}=0.1 mm/s. Panel a and b correspond to 0.1 m and 1 m thick soft faults, respectively. We utilize the same code color as in Fig. 2 to delimit the fault and background regions.

in v_{eff} for higher frequencies. In spite of this, we have verified that the integral of v_{eff} from the fault's edge to a fixed distance to the fault is still larger for higher frequencies. In this regard, Candela et al. (2015) showed that this integral is indicative of the overall expected permeability enhancement, which, for frequencies between 0.05 Hz and 1 Hz, was positively correlated with frequency. These results indicate that seismically-induced unclogging should preferentially occur in the vicinity of the fault's edge and that the corresponding effects should increase with the frequency.

An interesting feature of Fig. 7 is that v_{eff} is not continuous across the fault's interfaces. The reason for this is that although Darcy velocity is continuous across the fault interfaces (Deresiewicz & Skalak, 1963), different porosity values in the fault and in the background are used to compute v_{eff} (Eq. 10). This also explains the increase in v_{eff} at $y = H_{fault}$ from the fault towards the background medium. On the other hand, the lower v_{eff} at $y = H_{fault}$ compared with $y = 0$ m is due to the loss of P-wave seismic energy inside the fault zone mainly related to the energy split prevailing at the interface $y = 0$ m.

3.3 P- and S-wave oblique incidence

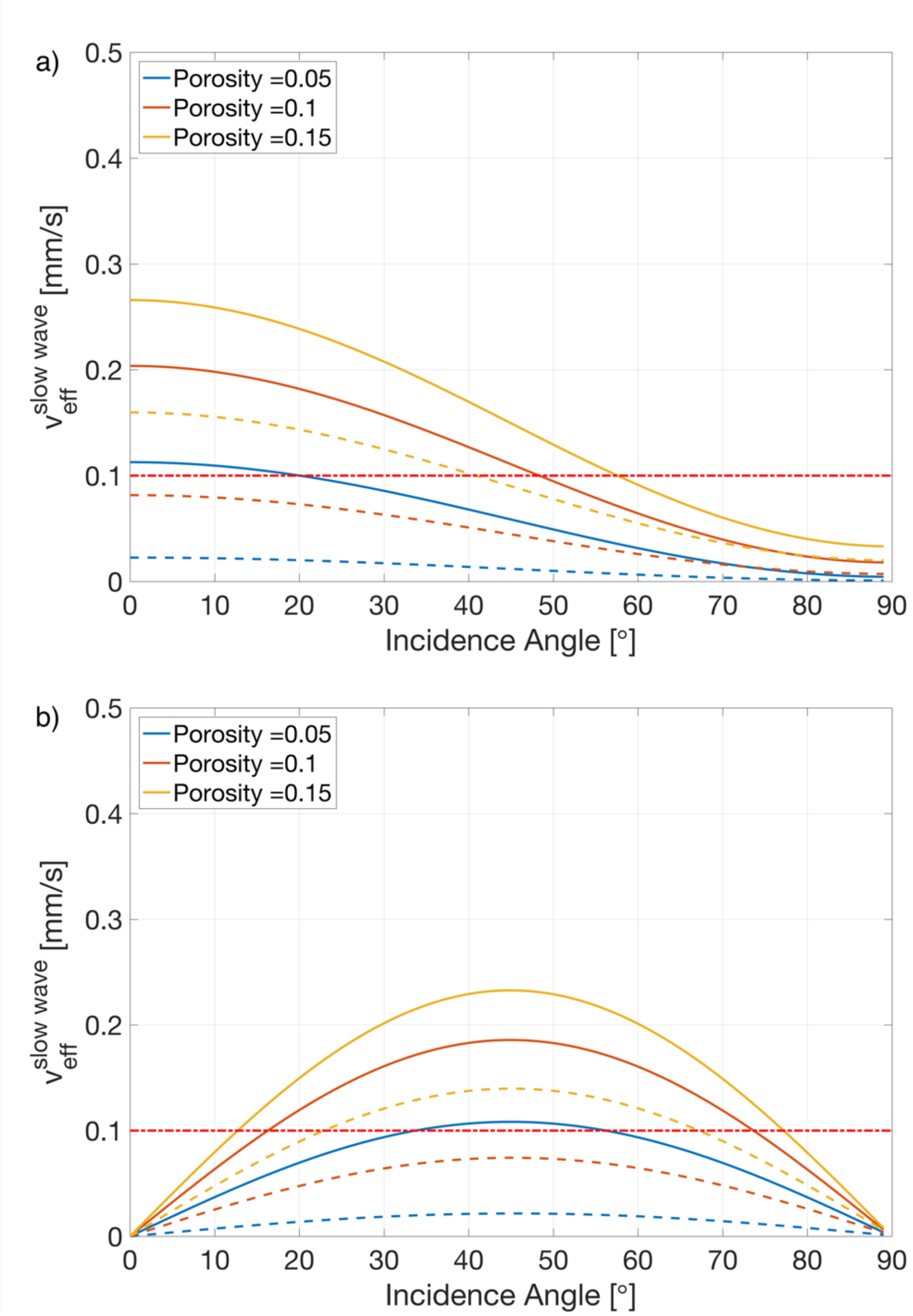

Figure 8. Effective pore velocity at the edge of the fault as a function of a) P- and b) S-wave incidence angle. Frequency is fixed at 1 Hz. We consider a 1 m-thick soft fault. The red dashed line denotes the threshold value of v_{eff}=0.1 mm/s.

Fig. 8 extends the analysis of Section 3.2 to P- and S-wave oblique incidence. In order to compare v_{eff} for different directions of wave propagation, we consider that the strain associated with a seismic wave is the same for all incidence angles and equal to 1e-5. For P- and S-waves, this condition implies a fixed extensional and shear strain, respectively, in the direction of wave propagation. For the analysis, we consider the soft fault of 1 m thickness and fixed the frequency to 1 Hz. We compute the seismically-induced v_{eff} at the edge of the fault located at $y = 0$ m in Fig. 2. Finally, only the y-component of the Darcy velocity ($\dot{w}_y$) is used to compute v_{eff} as the diffusion process associated with the slow P-waves is mainly normal to the fault's plane (Barbosa et al., 2017) and thus $\dot{w}_x \to 0$. Fig. 8a shows that, for P-wave incidence, v_{eff} decreases as the incidence angle gets closer to the horizontal direction (parallel to the fault). This is due to the decreased compression imposed by the incident wave and consequent reduction of the induced pressure gradient between the fault and the background medium. The inflection point of the angle dependence occurs at 45° for all cases. Nevertheless, for the case of 0.15 porosity, v_{eff} is above v^0_{eff} for incidence angles up to around 55°. Fig. 8b shows v_{eff} induced by the incidence of S-waves at different angles. In this case, maximal unclogging potential is reached at intermediate incidence angles (∼45°). Comparing the cases of 0.15 porosity for P-wave and S-wave incidence shows that S-waves can produce $v_{eff} > v^0_{eff}$ over a larger range of angles ($\sim 12.5°$ to $\sim 77.5°$).

4 Discussion

4.1 Pore scale heterogeneities

We have used Eq. 10 to compute the effective pore velocity as a result of the fluid flow associated with slow P-waves diffusing in a fault zone. For homogeneous media (e.g., background medium in our model), v_{eff} given by Eq. 10 is the sum of all pore velocities (averaged over the pore radius) divided by the number of pores. If all pores have the same radius, the computed effective velocity is the same as the individual pore velocities. However, when the medium exhibits a non-uniform pore radius distribution, the link between the estimated Darcy velocity and the actual pore fluid velocities is more complex than the one given in Eq. 10. One way to account for such heterogeneity is by considering a pore radius distribution for the medium and analyze which pores are more sensitive to the transient flow and thus more prone to be unclogged. Let us assume that the pore space of the medium can be conceptualized as a network of capillary tubes that are subjected to the same seismically-induced pressure gradient. The Hagen-Poiseuille flow solution for the average fluid velocity in a pore of radius r is given by

$$v_{pore}(r) = \frac{|\nabla p_f| r^2}{8\eta}. \tag{16}$$

By imposing v_{pore}=0.1 mm/s and using the pressure gradients associated with the slow P-waves created by the incidence of a body wave to a fault, we can compute the minimum radius (r_{min}) for which the pore velocity threshold is reached.

Fig. 9 shows the pore throat distribution for a Berea sandstone estimated by Dong and Blunt (2009). The two sets of dots correspond to two different methods to extract pore networks from micro-CT 3D images. The porosity of the sample used by Dong and Blunt (2009) is around 0.19. In Fig. 9, we also show the minimum radius (r_{min}) at which the transient flow associated with the diffusive waves exceeds v^0_{pore}=0.1 mm/s. Given that ∇p_f depends on the frequency, we have computed r_{min} at f=0.1, 1, 10 Hz. In Fig. 9 we consider the case of 0.15 porosity as it is the closest one to the sample of Dong and Blunt (2009) and the rest of the properties of the model correspond to those used in Fig. 5b.

We observe that as the frequency increases, r_{min} decreases. In other words, a larger number of pores exhibit $v_{pore} > v^0_{pore}$. According to Fig. 5b, in the background medium,

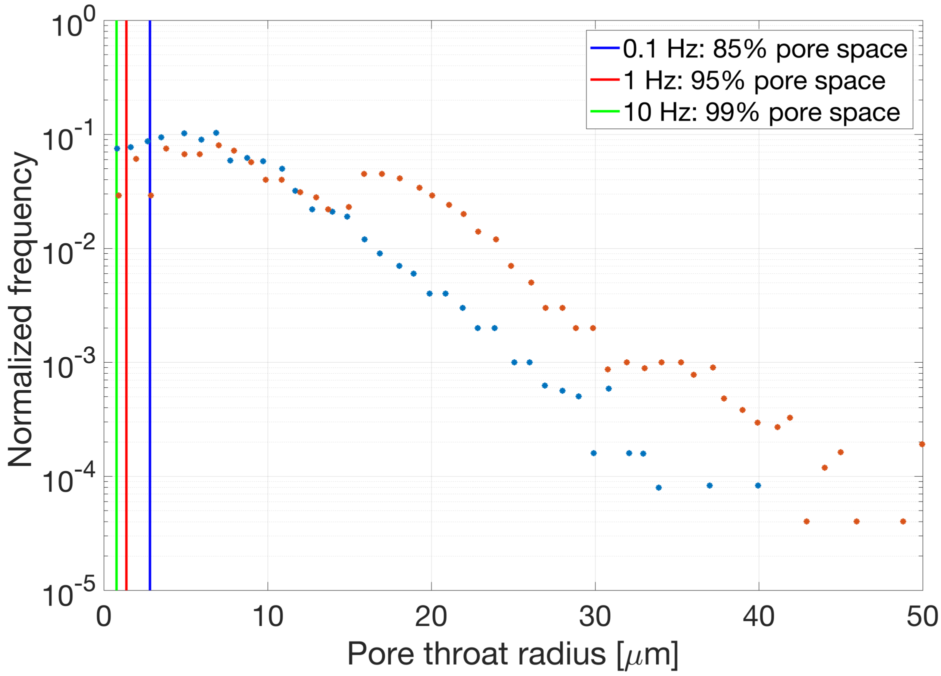

Figure 9. Pore throat radius distribution for a Berea sandstone of 0.19 porosity (Dong & Blunt, 2009). Vertical lines indicate the minimum radius r_{min} at which $v_{pore} > v^0_{pore}$ for three frequencies. These radii are used to compute the percentage of the pore space satisfying the condition $v_{pore} > v^0_{pore}$.

$v_{eff} > v^0_{eff}$ at 1 Hz but not at 0.1 Hz. From the pore radius distribution and the r_{min} estimates at 0.1 Hz and 1 Hz, we get that at 0.1 Hz, the condition $v_{pore} > v^0_{pore}$ is met for 85% of the pores. For a frequency of 1 Hz, on the other hand, the condition is met for 95% of the pore space. Interestingly, Fig. 9 shows that although for 0.1 Hz the condition $v_{eff} > v^0_{eff}$ is not met at the macro-scale, a significant portion of the pore space may still be affected by unclogging.

4.2 Mesoscale heterogeneities

The problem studied in this work represents a case of mesoscopic FPD in the sense that it deals with body wave energy conversion at the interfaces of a fault to diffusive slow P-waves. However, fault zones may also be highly heterogeneous at the mesoscale. Typical fault structures exhibit a fault core and a highly fractured damage zone surrounded by intact host rock (Fig. 2b). In this work, we have assumed that seismic wave frequencies are low enough so that the fluid pressure has enough time to equilibrate internally between the different regions in the fault zone. Consequently, the fault has been represented with an effective poroelastic medium for which an average response to the incidence of a body wave is modeled. In the simplest case of a damage zone composed by parallel fractures, for example, the "relaxed" assumption is valid as long as the diffusion length in the fault is much larger than the characteristic aperture and separation of the fractures (Gurevich, 2003). For the fault diffusivities and frequencies considered in this work, the low-frequency approximation is valid as long as the spacing between fractures within the damage zone of the fault is in the order of tens of centimeters or smaller.

In a more general scenario, when a seismic wave propagates through a region of the fault containing fractures, the compressibility contrast between fractures and the embedding rock can cause the development of additional pressure gradients and FPD. Pride and Berryman (2003) developed a so-called double-porosity analytical model, which consists of a mixture of two dissimilar porous phases (e.g., host rock and fractures) that behaves isotropically as a whole. They showed that when one porous phase is fully embedded in the other one, which is typically the case in fractured media, the double porosity model can be reduced to the classical "single-porosity" theory (set of Eqs. 1). In such case, the drained and undrained moduli as well as the Biot effective stress coefficient become complex-valued to allow for mesoscopic FPD between the fractures and the embedding background medium, herein referred to as fracture-to-background FPD (FB-FPD). Moreover, an effective permeability of the fractured medium is used in Darcy's law (Eq. 1d). If, in addition, the fracture network contains hydraulically connected fractures, seismic waves can induce heterogeneous fluid pressure response within connected fractures depending on their orientation and compliance contrast. Recently, Barbosa, Hunziker, et al. (2019) showed that for seismic wave characteristics similar to those considered in this work, mesoscopic FPD associated with seismically-induced pressure gradients between connected fractures (i.e., fracture-to-fracture FPD or FF-FPD) can be sufficiently strong to initiate unclogging within the fractures. The equations governing seismic wave propagation used in this work (set of Eqs. 1), ignore any FB- and FF-FPD effects occurring inside the fault zone as well as their impact on the scattered waves at the fault interfaces. Nevertheless, our results represent order-of-magnitude estimates of the effects that diffusive waves can have in faults and a generalization of the fault reflectivity problem accounting for other mesoscopic FPD effects will be part of future studies.

4.3 Reservoir scale heterogeneities

The fault model considered in this work represents a single fault embedded in a homogeneous rock formation. The effects that body waves can have on faults and the associated unclogging potential can be affected by additional structural complexity in the model such, as for example, the presence of anticlines and piercement geological structures that may act like acoustic lenses focusing and amplifying the incoming seismic energy (Davis et al., 2000; Lupi, Frehner, et al., 2017). Such effects are particularly influenced by the impedance contrast between rock formations as well as by the geometrical characteristics of the subsurface structures. In addition, fault systems often exhibit multiple faults whose elastic and hydraulic interaction may also affect their seismic response. Ultimately, these factors may operate on the frequency content, seismic energy density, and incidence angle of the waves arriving at the fault of interest, which, as shown in this work, strongly affect the fault unclogging potential. Investigating the associated processes requires numerical simulations of wave propagation in poroelastic media at the reservoir or basin scale that are able to handle the large range of feature scales that may be present in the model. This kind of study requiring tailored geological models, which is computationally challenging, is beyond the scope of our work. Finally, seismically-induced permeability changes have been typically associated with teleseismic events and consequently with the propagation of long-period surface waves (Brodsky et al., 2003; Wang & Manga, 2010; Manga et al., 2012). Extending our analysis to the propagation of surface waves across fault zones will be part of our future studies.

5 Conclusions

Seismically-induced unclogging of pore spaces is one of the mechanisms of permeability changes in fluid-saturated porous media typically evoked to explain the co-seismic hydrogeological response of reservoirs. In this work, we have investigated the potential of seismic body waves to induce sufficiently strong fluid flow in fault zones to unclog the pore space. We first showed that relative permeability changes through unclogging typically observed in laboratory experiments are associated with slow P-waves while effects associated with the propagation of classical body waves are largely negligible.

We have shown that the unclogging potential of a fault zone that is subjected to the dynamic deformation imposed by P- and S-waves strongly depends on the incoming energy density, incidence angle, and frequency of the seismic waves as well as on the compliance and thickness of the fault zone. Depending on the combined effect of these properties, pressure gradients associated with slow P-waves created after the passage of body waves across faults can be several orders of magnitude higher than typical natural pressure gradients in the subsurface. Inside highly conductive faults, seismically-induced pressure gradients diffusing towards the interior of the fault are smaller than those diffusing towards the embedding background medium. This result suggests that unclogging is more likely to be more efficient removing blockages in the surrounding background than inside the fault.

For a given incoming seismic wave energy density, the unclogging potential always increases with the frequency. Our results imply that, for frequencies between 0.1 and 20 Hz, incident seismic energy densities of the order of 0.1 J/m^3 to 1 J/m^3 (i.e., strains close to 1e-5) are necessary for unclogging to be expected both inside the fault and in the embedding background medium. Seismically-induced pressure gradients of the order of hundreds of kPa/m are generally necessary to reach the minimum pore velocities to unclog a significant portion of the pore space. As a consequence, faults exhibiting mild to low stiffness contrast with respect to the intact host rock are not likely to experience unclogging. We have also shown that the energy conversion from incident P- and S-waves to slow P-waves at the edge of the fault strongly depends on the ratio between the incident wavelength and the thickness of the fault. In general, this dependence implies that thicker fault sections are more prone to unclogging than thinner ones provided they have the same petrophysical properties.

Finally, for P-wave incidence, the unclogging potential decreases as the incidence angle gets closer to parallel to the fault plane as the deformation imposed by the P-wave to the fault decreases. S-waves, on the other hand, induce maximal pressure gradients between the fault and its surroundings at intermediate angles of incidence. For equal imposed strains, the maximal effective pore velocities induced by P- and S-waves are similar. However, the range of incidence angles at which the effective pore velocities is above the unclogging threshold of 0.1 mm/s is larger for S-waves than for P-waves.

Acknowledgments

This work was supported by a grant from the Swiss National Science Foundation (GENERATE, Grant number 166900) and completed within the SCCER-SOE framework. The data for this paper are available at `http://doi.org/10.5281/zenodo.3817529`.

References

Bai, R., & Tien, C. (1997). Particle detachment in deep bed filtration. *Journal of colloid and interface science*, *186*(2), 307–317.

Barbosa, N. D., Caspari, E., Rubino, J. G., Greenwood, A., Baron, L., & Holliger, K. (2019). Estimation of fracture compliance from attenuation and velocity analysis of full-waveform sonic log data. *Journal of Geophysical Research: Solid Earth*, *124*(3), 2738–2761.

Barbosa, N. D., Hunziker, J., Lissa, S., Saenger, E. H., & Lupi, M. (2019). Fracture unclogging: A numerical study of seismically induced viscous shear stresses in fluid-saturated fractured rocks. *Journal of Geophysical Research: Solid Earth*.

Barbosa, N. D., Rubino, J. G., Caspari, E., & Holliger, K. (2017). Extension of the classical linear slip model for fluid-saturated fractures: Accounting for fluid pressure diffusion effects. *Journal of Geophysical Research: Solid Earth*, *122*(2), 1302–1323.

Barbosa, N. D., Rubino, J. G., Caspari, E., Milani, M., & Holliger, K. (2016). Fluid pressure diffusion effects on the seismic reflectivity of a single fracture. *The Journal of the Acoustical Society of America*, *140*(4), 2554–2570.

Bedrikovetsky, P., Zeinijahromi, A., Siqueira, F. D., Furtado, C. A., & de Souza, A. L. S. (2012). Particle detachment under velocity alternation during suspension transport in porous media. *Transport in Porous Media*, *91*(1), 173–197.

Bergendahl, J., & Grasso, D. (2000). Prediction of colloid detachment in a model porous media: Hydrodynamics. *Chemical Engineering Science*, *55*(9), 1523–1532.

Berryman, J. G., & Wang, H. F. (2000). Elastic wave propagation and attenuation in a double-porosity dual-permeability medium. *International Journal of Rock Mechanics and Mining Sciences*, *37*(1-2), 63–78.

Biot, M. A. (1962). Mechanics of deformation and acoustic propagation in porous media. *Journal of Applied Physics*, *33*, 1482-1498.

Bourbié, T., Coussy, O., & Zinszner, B. (1987). *Acoustics of porous media.* Editions Technip.

Brehme, M., Regenspurg, S., Leary, P., Bulut, F., Milsch, H., Petrauskas, S., . . . Blöcher, G. (2018). Injection-triggered occlusion of flow pathways in geothermal operations. *Geofluids*.

Brodsky, E. E., & Prejean, S. G. (2005). New constraints on mechanisms of remotely triggered seismicity at long valley caldera. *Journal of Geophysical Research: Solid Earth*, *110*(B4).

Brodsky, E. E., Roeloffs, E., Woodcock, D., Gall, I., & Manga, M. (2003). A mechanism for sustained groundwater pressure changes induced by distant earthquakes. *Journal of Geophysical Research: Solid Earth*, *108*(B8).

Candela, T., Brodsky, E. E., Marone, C., & Elsworth, D. (2014). Laboratory evidence for particle mobilization as a mechanism for permeability enhancement via dynamic stressing. *Earth and Planetary Science Letters*, *392*, 279–291.

Candela, T., Brodsky, E. E., Marone, C., & Elsworth, D. (2015). Flow rate dictates permeability enhancement during fluid pressure oscillations in laboratory experiments. *Journal of Geophysical Research: Solid Earth*, *120*(4), 2037–2055.

Chen, X., Wu, Z., Cai, Q., & Cao, W. (2018). Effect of ultrasonic stimulation on particle transport and fate over different lengths of porous media. *Journal of hydrology*, *559*, 972–983.

Cheng, A. H.-D. (2016). *Poroelasticity* (Vol. 27). Springer.

Chester, F. M., Evans, J. P., & Biegel, R. L. (1993). Internal structure and weakening mechanisms of the san andreas fault. *Journal of Geophysical Research: Solid Earth*, *98*(B1), 771–786.

Davis, P. M., Rubinstein, J. L., Liu, K. H., Gao, S. S., & Knopoff, L. (2000). Northridge earthquake damage caused by geologic focusing of seismic waves. *Science*, *289*(5485), 1746–1750.

Deresiewicz, H., & Skalak, R. (1963). On uniqueness in dynamic poroelasticity. *Bulletin of the Seismological Society of America*, *53*(4), 783–788.

Dong, H., & Blunt, M. J. (2009). Pore-network extraction from micro-computerized-tomography images. *Physical review E*, *80*(3), 036307.

Elkhoury, J. E., Brodsky, E. E., & Agnew, D. C. (2006). Seismic waves increase permeability. *Nature*, *441*(7097), 1135.

Elkhoury, J. E., Niemeijer, A., Brodsky, E. E., & Marone, C. (2011). Laboratory observations of permeability enhancement by fluid pressure oscillation of in situ fractured rock. *Journal of Geophysical Research: Solid Earth*, *116*(B2).

Faulkner, D., Mitchell, T., Jensen, E., & Cembrano, J. (2011). Scaling of fault damage zones with displacement and the implications for fault growth processes. *Journal of Geophysical Research: Solid Earth*, *116*(B5).

Guglielmi, Y., Cappa, F., Avouac, J.-P., Henry, P., & Elsworth, D. (2015). Seismicity triggered by fluid injection–induced aseismic slip. *Science*, *348*(6240), 1224–1226.

Gurevich, B. (2003). Elastic properties of saturated porous rocks with aligned fractures. *Journal of Applied Geophysics*, *54*(3), 203–218.

Gurevich, B., Marschall, R., & Shapiro, S. (1994). Effect of fluid flow on seismic reflections from a thin layer in a porous medium. *Journal of Seismic Exploration*, *3*(2), 125–140.

Gurevich, B., & Schoenberg, M. (1999). Interface conditions for Biot's equations of poroelasticity. *The Journal of the Acoustical Society of America*, *105*(5), 2585-2589.

Hobday, C., & Worthington, M. (2012). Field measurements of normal and shear fracture compliance. *Geophysical Prospecting*, *60*(3), 488–499.

Huenges, E., Ellis, J., Welter, S., Westaway, R., Min, K.-B., Genter, A., ... Marti, M. (2018). *Demonstration of soft stimulation treatments in geothermal reservoirs.*

Jeanne, P., Guglielmi, Y., Rutqvist, J., Nussbaum, C., & Birkholzer, J. (2017). Field characterization of elastic properties across a fault zone reactivated by fluid injection. *Journal of Geophysical Research: Solid Earth*, *122*(8), 6583–6598.

Johnson, D. L., Koplik, J., & Dashen, R. (1987). Theory of dynamic permeability and tortuosity in fluid-saturated porous media. *Journal of fluid mechanics*, *176*, 379–402.

Kim, Y.-S., & Sanderson, D. J. (2005). The relationship between displacement and length of faults: a review. *Earth-Science Reviews*, *68*(3-4), 317–334.

Kocharyan, G., Vinogradov, E., Gorbunova, E., Markov, V., Markov, D., & Pernik, L. (2011). Hydrologic response of underground reservoirs to seismic vibrations. *Izvestiya, Physics of the Solid Earth*, *47*(12), 1071–1082.

Kutay, M. E., & Aydilek, A. H. (2009). Pore pressure and viscous shear stress distribution due to water flow within asphalt pore structure. *Computer-Aided Civil and Infrastructure Engineering*, *24*(3), 212–224.

Lay, T., & Wallace, T. C. (1995). *Modern global seismology.* Elsevier.

Li, X., Zhang, P., Lin, C., & Johnson, W. P. (2005). Role of hydrodynamic drag on microsphere deposition and re-entrainment in porous media under unfavorable conditions. *Environmental science & technology*, *39*(11), 4012–4020.

Liu, W., & Manga, M. (2009). Changes in permeability caused by dynamic stresses in fractured sandstone. *Geophysical Research Letters*, *36*(20).

Lupi, M., Frehner, M., Weis, P., Skelton, A., Saenger, E. H., Tisato, N., ... Driesner, T. (2017). Regional earthquakes followed by delayed ground uplifts at campi flegrei caldera, italy: Arguments for a causal link. *Earth and Planetary Science Letters*, *474*, 436–446.

Lupi, M., Fuchs, F., & Saenger, E. H. (2017). Numerical simulations of passing seismic waves at the larderello-travale geothermal field, italy. *Geophysical Research Letters*, *44*(11), 5418–5426.

Lupi, M., Saenger, E. H., Fuchs, F., & Miller, S. (2013). Lusi mud eruption triggered by geometric focusing of seismic waves. *Nature Geoscience*, *6*(8), 642.

Manga, M., Beresnev, I., Brodsky, E. E., Elkhoury, J. E., Elsworth, D., Ingebritsen, S. E., ... Wang, C.-Y. (2012). Changes in permeability caused by transient stresses: Field observations, experiments, and mechanisms. *Reviews of geophysics*, *50*(2).

Müller, T. M., Gurevich, B., & Lebedev, M. (2010). Seismic wave attenuation and dispersion resulting from wave-induced flow in porous rocks—a review. *Geophysics*, *75*(5), 75A147–75A164.

Müller, T. M., & Rothert, E. (2006). Seismic attenuation due to wave-induced flow: Why Q in random structures scales differently. *Geophysical Research Letters*, *33*(16).

Parsons, T., Malagnini, L., & Akinci, A. (2017). Nucleation speed limit on remote fluid-induced earthquakes. *Science Advances*, *3*(8), e1700660.

Pride, S. R. (2005). Relationships between seismic and hydrological properties. In *Hydrogeophysics* (pp. 253–290). Springer.

Pride, S. R., & Berryman, J. G. (2003). Linear dynamics of double-porosity dual-permeability materials. I: governing equations and acoustic attenuation. *Physical Review E*, *68*(3), 036603-1–10.

Pride, S. R., Berryman, J. G., & Harris, J. M. (2004). Seismic attenuation due to wave-induced flow. *Journal of Geophysical Research: Solid Earth*, *109*(B1).

Pride, S. R., Flekkøy, E. G., & Aursjø, O. (2008). Seismic stimulation for enhanced oil recovery. *Geophysics*, *73*(5), O23–O35.

Roberts, P. M. (2005). Laboratory observations of altered porous fluid flow behavior in berea sandstone induced by low-frequency dynamic stress stimulation. *Acoustical Physics*, *51*(1), S140–S148.

Roberts, P. M., & Abdel-Fattah, A. I. (2009). Seismic stress stimulation mobilizes colloids trapped in a porous rock. *Earth and Planetary Science Letters*, *284*(3-4), 538–543.

Savage, H. M., & Brodsky, E. E. (2011). Collateral damage: Evolution with displacement of fracture distribution and secondary fault strands in fault damage zones. *Journal of Geophysical Research: Solid Earth*, *116*(B3).

Shi, Y., Liao, X., Zhang, D., & Liu, C.-p. (2019). Seismic waves could decrease the permeability of the shallow crust. *Geophysical Research Letters*.

Shi, Z., Zhang, S., Yan, R., & Wang, G. (2018). Fault zone permeability decrease following large earthquakes in a hydrothermal system. *Geophysical Research Letters*, *45*(3), 1387–1394.

Shokouhi, P., Jin, J., Wood, C., Riviere, J., Madara, B., Elsworth, D., & Marone, C. (2019). Dynamic stressing of naturally fractured rocks: on the relation between transient changes in permeability and elastic wave velocity. *Geophysical Research Letters*.

Van Der Elst, N. J., & Brodsky, E. E. (2010). Connecting near-field and far-field earthquake triggering to dynamic strain. *Journal of Geophysical Research: Solid Earth*, *115*(B7).

Wang, C.-Y., Chia, Y., Wang, P.-l., & Dreger, D. (2009). Role of s waves and love waves in coseismic permeability enhancement. *Geophysical Research Letters*, *36*(9).

Wang, C.-Y., & Manga, M. (2010). Hydrologic responses to earthquakes and a general metric. *Geofluids*, *10*(1–2), 206–216.

White, J. E., Mihailova, N., & Lyakhovitsky, F. (1975). Low-frequency seismic waves in fluid-saturated layered rocks. *The Journal of the Acoustical Society of America*, *57*(S1), S30–S30.

Xue, L., Li, H.-B., Brodsky, E. E., Xu, Z.-Q., Kano, Y., Wang, H., … Zhang, W. (2013). Continuous permeability measurements record healing inside the wenchuan earthquake fault zone. *Science*, *340*(6140), 1555–1559.

Zang, A., Zimmermann, G., Hofmann, H., Stephansson, O., Min, K.-B., & Kim, K. Y. (2019). How to reduce fluid-injection-induced seismicity. *Rock mechanics and rock engineering*, *52*(2), 475–493.